Hysterons and pathways in mechanical metamaterials
Ding, J.

SEQUENTIAL SNAPPING AND PATHWAYS IN A BIHOLEY METAMATERIAL [1]

3.1 Introduction and motivation

Bistable, hysteretic elements commonly occur in complex materials and play a key role in the understanding of memory effects [16–18, 20, 21, 27, 28, 40, 42, 44–47, 49, 50, 56–58]. Intuitively, when cyclically driving a complex system, one imagines these elements to undergo sequences of flipping transitions associated with hopping between metastable states. To understand these sequences, it is often possible to model these bistable elements as hysterons: hysteretic elements which which flip their internal state s from '0' to '1' when the local driving exceeds the upper switching field ε^+, and which flip from '1' to '0' when the driving falls below the lower switching field ε^- (Fig. 1a) [17, 21, 44, 46, 47, 49]. By specifying the values of the switching fields of a collection of hysterons, and potentially their interactions, one can determine the transitions between all collective states $S := \{s_1, s_2, \dots\}$, and represent these in a transition graph (t-graph) which takes the form of a directed (multi)graph [17, 18, 44–48]. The (topological) organization of such t-graphs characterize the complex response of complex media and in particular memory effects such as Return Point Memory

---

[1] A version of this chapter was published as [56].

(RPM), transient memories, and subharmonic response [17, 44–48, 50, 57–60].

Controlling, characterizing and manipulating such hysterons is challenging in disordered systems such as crumpled sheets and amorphous media [18, 40, 61–65]. Here we propose instead to leverage the design freedom of mechanical metamaterials to embed hysterons into a flexible metamaterial [1, 16, 20, 27, 28, 42, 66]. This allows to control and tune their switching fields and to directly observe the sequences of hysteron flipping that constitute the deformation pathways and yield the t-graph. Developing such metamaterial platforms is an important step towards achieving materials with deformation pathways on demand [4, 67], with targeted memory properties and specific responses to cyclical driving, and with advanced pathways that include elementary computations. Moreover, such metamaterials allow to explore generality and robustness of the hysteron picture, and to more closely explore the material properties (e.g. sensitivity to boundary conditions) of multistable materials. Finally, metamaterials allow to explore the interactions between non-discrete degrees of freedom, for example given by visco-plastic relaxation and solid-on-solid friction, which may lead to additional timescales and continuous degrees of freedom not considered in simple hysteron models [40].

Here we introduce a simple metamaterial platform in which mechanical hysterons with controllable switching fields can be embedded. We start from the well-known biholar metamaterials, which translate global uniaxial compression to local rotation and compression [2, 3, 30]. We then leverage the hysteretic snapping of beams between left- and right buckled states to locally replace slender elements of the metamaterial by hybrid pusher-beam elements[1, 16, 19, 20, 27, 28, 42]. We show that tuning their design parameters allows to access qualitatively different pathways. Moreover, we use gradients in the boundary conditions to independently tune the effective switching fields of the hysterons, thus obtaining multiple pathways from a single sample [18]. Finally, we show how subtle frictional effects allow to slowly evolve the switching fields, giving rise to a history dependent response beyond that captured by simple hysteron models. Together,

our work opens new directions for the experimental study and control of multistable materials.

3.2 Phenomenology

The biholey design consists of alternating smaller and larger holes, separated by precurved, hourglass-shaped beams which are connected in groups of four in diamond shaped islands (Fig. 3.2 (a)) [2, 3, 11, 30, 34–39] (see Section 1.3). Under vertical compression, the biholey metamaterial forms a pattern of alternating horizontal and vertical ellipse, and the diamond shaped islands exhibit counter-rotating motion [2, 3, 11, 30, 34–39].

What if we replace an hourglass shaped beam with a slender beam that curved to the opposite direction to the hourglass shaped beam? As we have shown in Chapter 2, for appropriate designs this 'defect' beam can undergo a snap transition. In this section, we investigate the possible behavior of multiple slender defect beams in a biholey metamaterial experimentally.

To investigate the snapping (or unsnapping) behavior, each defect, which act as as hysteron (Section 3.4), is composed of a defect beam with curvature opposite to that expected in the biholar design, and a set of pushers. This design ensures that under compression the defect beam will be pushed by these pushers from its initially curved state to a snapped, oppositely curved state. Such pushers are not strictly necessary (Chapter 2), but facilitate robust snapping in experiment. Under decompression, the defect beam then snaps back to its initially curved state. We label the unsnapped and snapped states of the defect beam as $'s = 0'$ and $'s = 1'$, to stress that the defect beam acts as a mechanical hysteron [18, 58]. We track the compressive strain (Section 1.2), ε, and follow the evolution of s. Fig. 3.1 shows an example of the evolution of the hysterons in a sample under cyclic compression. From left to the right, we label the hysterons as 1, 2, and 3. The collective state, S, is characterized by all the states of the hysterons $\{s_1, s_2, s_3\}$.

Fig. 3.1 (a) shows the initial state of the sample ($\varepsilon = 0$) where all defect beams are in their unsnapped state, i.e. curving to the left. As the strain increases, the defect beams initially curve more to the left. However, the overall deformation and local rotations inside the biholar metamaterial are incompatible with the deformations of the defect beams, and the two end points of these beams in fact rotate counter to the bending of the defect beams. Hence frustration builds up, and the hysterons are prone to snapping. To facilitate this further, we have inserted "pushers" into the sample, that make contact with the defect beams and push them towards snapping (Chapter 2). The middle beam, beam 2, first snaps at $\varepsilon = 0.237 \pm 0.002$[2], as shown in Fig. 3.1 (b), and we get a new state $\{010\}$. By continuing compressing the sample, the beam 1 snaps when $\varepsilon \geq 0.270$ and we get the new state $\{110\}$. When $\varepsilon \geq 0.289$, beam 3 snaps and we reach the new state $\{111\}$.

Next we slowly decompress the sample to see the unsnapping behavior of the beams. For this sample, the beams unsnaps in the same sequence as snap: first beam 2, next beam 1 and then beam 3. We will refer to the snapping and unsnapping strains of each beam i as ε_i^+ for snapping, and ε_i^- for unsnapping – if needed, we also will give the state before the (un)snapping event. As an example, instead of $\varepsilon_{111 \rightarrow 101}$, we write $\varepsilon_2^-(111)$. We get the unsnapping strain: $\varepsilon_2^-(111) = 0.047$, $\varepsilon_1^-(101) = 0.043$, $\varepsilon_3^-(001) = 0.029$.

There are many factors affect the ε^+ and ε^- of the multi beam system. We note that the beams do not snap together; and that for each beam, ε^+ always larger than ε^-. In the following sections, we will investigate the sequences of snapping and unsnapping events, which we call it pathway, in such systems. Our goal is to obtain samples with more complex pathways – for example, with different orderings for the snapping and unsnapping sequences – and to find design rules to control these sequences. The outline of this chapter is as follows. In section 3.3, we show the geometry of the sample and the method we used to study the (un)snapping behavior. In section 3.4, we investigate the snapping behavior of a single hysteron and the method to tune the (un)snapping strains. In section 3.5 and section 3.6,

---

[2]The error bar, 0.002, is govered by our frame rate (2 fps).

we discuss the transition pathways and the method to tune the pathways. In section 3.7, we show memory effects in our system, characterized by the ability of details of the driving history, such as the number of driving cycles, to influence the pathways.
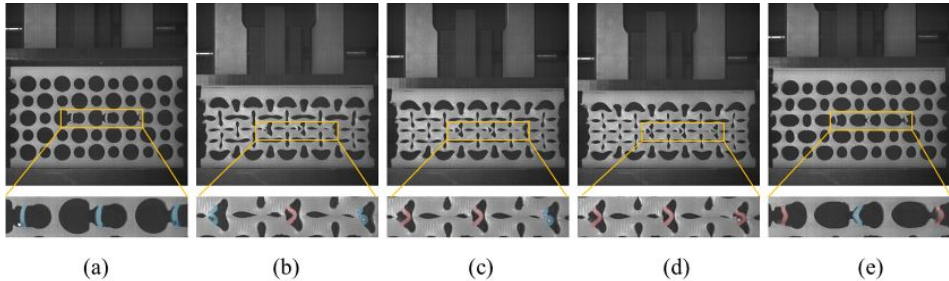

FIGURE 3.1: Evolution of the defect hysterons in a biholey sample under cyclic compression. In the zoom-ins, we show the hysterons 1, 2 and 3 (from left to right), with the color highlighting their state: blue denotes the unsnapped state $s = 0$, red denotes the snapped state $s = 1$. Corresponding strains and the states of the sample shown in (a - e) are as follows: (a) $\varepsilon = 0$, $S = \{000\}$; (b) $\varepsilon = 0.237$, $S = \{010\}$; (c) $\varepsilon = 0.270$, $S = \{110\}$; (d) $\varepsilon = 0.289$, $S = \{111\}$; (e) $\varepsilon = 0.047$, $S = \{101\}$. For more, see Appendix.

3.3 Geometry and approach

In this Section, we introduce the geometry and experimental method that we use to study the biholey system. In the sub-section 3.3.1, we introduce the optimized geometry design comparing to Chapter 2. In the sub-section 3.3.2 and sub-section 3.3.3, we introduce the methods of experimentation and data processing.
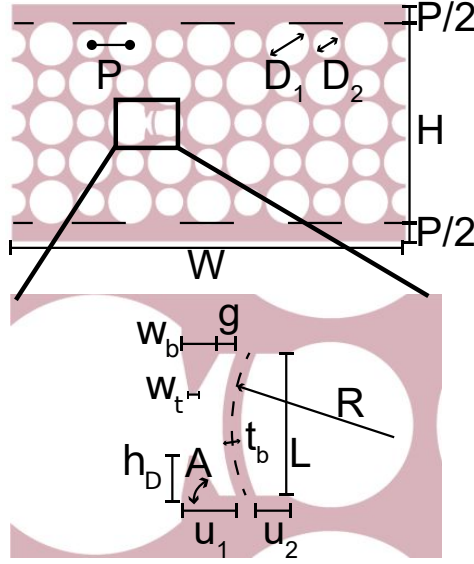
FIGURE 3.2: Quasi-2D biholey metamaterial of height $H = 50$ mm, width $W = 100$ mm and thickness $T = 18$ mm. The hole pattern has pitch $P = 10$ mm, the holes have diameters $D_1 = 11$ mm and $D_2 = 7$ mm. Zoom-in: geometry of the defect beam (not to scale). Here, $L = 6$ mm, and we fix the dimensionless radius of curvature $r := R/L = 0.8$, dimensionless thickness $t := t_b/L = 0.13$, and dimensionless location $u := \frac{u_1 - u_2}{u_1 + u_2} = 0$. The pushers are characterized by $\{g, A, w_t, w_b, h := h_D/L\} = \{0.7 \text{ mm}, 60°, 0.3 \text{ mm}, 1.6 \text{ mm}, 0.28 \}$.

3.3.1 Geometry

To control the pattern transformation of the metamaterial, we embed a hysteron in the biholey metamaterial. We focus here on biholey metamaterials consisting of 9×5 holes. We use thick samples ($T = 18$ mm) to prevent out-of-plane buckling. To control $\varepsilon^{\pm}$ more efficiently, we design a pair of pushers in the mechanical hysterons. The properties of the mechanical hysterons depend on the design of both the defect beam and the triangular pushers, as well as on its location in the metamaterial (Fig. 3.2). The pushers are characterized by the angle A, the width of their bases w_t and w_b, their dimensionless height $h := h_D/L$, and the gap g between pusher and beam. Based on exploratory experiments and finite element simulations, we fix

the biholey array parameters $\{P, D_1, D_2\} = \{10\text{mm}, 11\text{mm}, 7\text{mm}\}$, fix the beam parameters $\{L, r, t\} = \{6\text{mm}, 0.8, 0.13\}$, fix the pusher parameters $\{g, A, w_t, w_b\} = \{0.7\text{mm}, 60°, 0.3\text{mm}, 1.6\text{mm}\}$, and vary the dimensionless pusher height h and horizontal beam location u.

3.3.2 Experimental Procedure

We create our samples by 3D printing molds, and filling these with a two-component elastomer (Zhermack Elite Double 8, $E \approx 220$ kPa, $\nu \approx 0.5$). We place our sample in dual column Instron 5965 uniaxial compression device (resolution better than 4 μm) and measure the compressive forces (using a 100 N load cell yielding a resolution better than 0.5 mN) during cycling loading between compressive strains ε^m and ε^M.
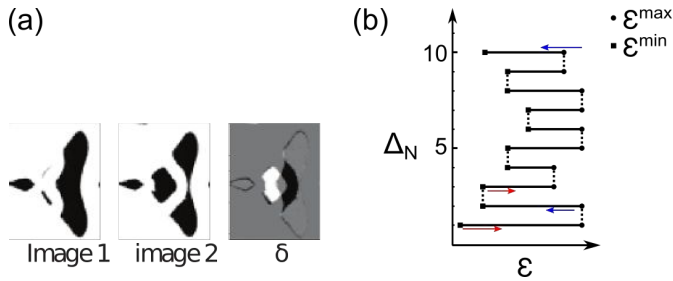

FIGURE 3.3: (a) An example of image analysis, where the images have enhanced contrast. and δ is a difference between two samples. (b) An example of cyclical loading process, where Δ_N denotes the driving sweeps.

The sample is clamped between the ground plate and top plate. The bottom plate can be tilted by $|\alpha| < \pm\, 0.5°$. To allow the sample to relax, we do not fix the top plate to the sample. To choose the compression where $\varepsilon = 0$, we use a linear fit to force vs compression curves for ε in the range between 0.1 and 0.4.

We apply cyclic loading using a (de)compression rate of 0.2 mm/sec, which leads to nearly quasistatic behavior — much faster rates lead to inertial effects, while much lower rates lead to creep effects. We obtain the strain, $\varepsilon := E_y/H$ and stress, $\sigma := F/(WT)$ of the sample from the displacement sensor and the force sensor, where E_y denotes the displacement of the top surface of the sample, and F is the compressive force.

We monitor the compressive force and in parallel use video imaging to capture the sample deformations as function of strain, using a Basler asA2040-25gm/gc CMOS camera (2048 × 2048 pixels, framerate 2 fps). To detect snapping events, we use difference imaging where the difference, δ, is defined as

$$\delta_k = \sum_{i,j}(\mathbf{I}_{k+1}(i,j) - \mathbf{I}_k(i,j))^2 \, , \tag{3.1}$$

where $\mathbf{I}_k(i,j)$ denotes the pixel array of frame k, as shown in Fig. 3.3 (a). To normalize these differences, we use Δ:

$$\Delta = \Delta_k + \Delta_N = \frac{\delta_k}{<\delta_k>} + \Delta_N, \tag{3.2}$$

where $< \delta >$ denotes the mean; Δ_N is the number of experimental loading steps, as show in Fig. 3.3 (b).

3.3.3 Onset fitting

When we start the experiment, the compression plate is a few millimeters away from the sample. To obtain a consistent definition of ε, we determine the onset point of compression by following the linear initial growth part of the stress - strain curve.

We first read the raw data in the compression process and using the Python package, scipy.interpolate.UnivariateSpline, to reduce the noise in the original data. Then we read a part of the initial growth part, where the stress is in the range 0.1 kPa $< \sigma <$ 0.35 kPa. Next we use the Python package scipy.optimize.curve_fit to fit the initial growth part to a line: $\sigma = au + u_0$,

where a is the slope of the line and u_0 is the onset point of compression, as shown by the black line in Fig. 3.4. In the following sections, the $\varepsilon - \sigma$ curve we show is the processed curve, where $\varepsilon = \frac{u - u_0}{H}$, as shown by the red curve in Fig. 3.4. We note that the value of $\varepsilon < 0$ does not imply that the sample is stretched, but rather that the compression plate does not reach the onset point of compression. In particular, for tilted samples, we also manually set the starting point of compression based on the linear fitting method.
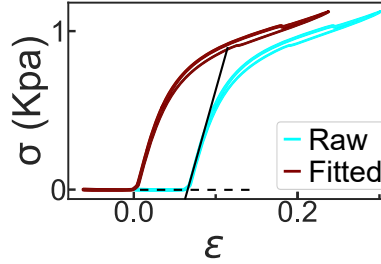

FIGURE 3.4: An example of onset fitting, where the sample is shown in Fig. 3.5. The dotted line denotes the line: '$\sigma = 0$'; the black line denotes the fitted line. For detail, see text.

3.4 (Un)snapping in biholey metamaterial

To facilitate snapping behavior, we have inserted "pushers" into the sample that push the defect beam under compression (Fig. 3.5a). We now focus on the behavior of a single mechanical hysteron.

We apply cyclic loading under compression by a strain $\varepsilon \lesssim 0.18$, the defect beam shown in Fig. 3.5a will initially bend left. In contrast, the rotation of the diamond shaped islands makes the tips of the pushers move right, so that they eventually come into contact with the defect beam. Further compression then causes a hysteretic transition of the defect beam into a right-snapped state at $\varepsilon^+ = 0.18$. To detect this transition we use difference imaging, which is sensitive to sudden motions, and define Δ as normalized
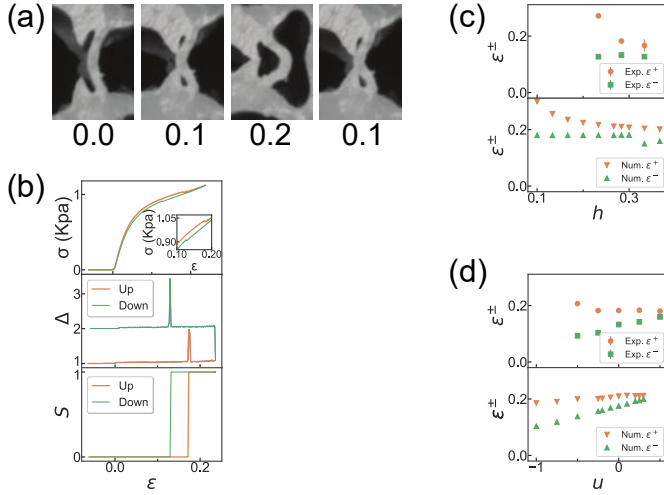
FIGURE 3.5: (a) Example of the evolution of the defect beam geometry under cyclic compression for the sample in Fig. 3.2, showing the pushers getting into contact of the beam and initiating a snapping toward the right. (b) Stress σ, image differences Δ, and hysteron state s as a function of strain ε for the sample in (b). Note that the image differences for compression and decompression are offset by one for visibility. (c) and (d) Critical switching strains $\varepsilon^{\pm}$ as a function of the dimensionless pusher height h and beam position u. We have performed three independent runs on two samples and calculated our error bar based on these six datasets.

difference of the snapshots of the defect snappers (see Eq. 3.2). We note that the snapping behavior, visible as a small but sharp drop in the compressive stress σ, can be seen very clearly in the image differences, and indicates that the hysteron state, s, switches from 0 to 1, as shown by the orange curve in Fig. 3.5b. Under decompression, the defect beam then snaps back to its left curved state at $\varepsilon^{-} = 0.13$, which can be seen in both the stress signal and the image differences (note that we have offset the image differences of the downsweep for clarity). We note that the ε^{+} is larger than ε^{-}, so that there is a bistable region, as expected for a hysteretic transition (Fig. 3.5 b).

We can modify the characteristic (un)snapping strains, $\varepsilon^{\pm}$, by modifying the design of the snappers, and focus on the role of the height of the pusher h and beam position u. We observe that ε^{+} increases for lower heights h

— more compression is needed to induce a snapping event with smaller pushers — whereas ε^- is essentially independent of h — which makes sense, as before unsnapping, the defect beam and pusher are not in contact (Fig. 3.5(c)). We note that our numerical results show a discontinuity for $h \sim 0.32$ — here the pushers are so high that two opposing pusher come into contact, hinder rotation of the diamonds above and below the defect beam, and delay the unsnapping transition. As a function of the relative defect beam position u, we observe that ε^+ is nearly constant, while ε^- increases with u (Fig. 3.5(d)). We interpret this trend as follows: due to rotation of the diamonds, the effective distance between top and bottom of the defect beam decreases when u is decreased; such defect beams are thus more compressed, and unsnap for lower values of ε. Finally we note that for extreme parameter choices, instead of snapping, the beam undergoes smooth deformations and stops acting as a hysteron; this occurs for example when $u > 0.5$. We conclude that the geometric parameters of the snapping beam allow to tune the upper and lower switching fields $\varepsilon^{\pm}$ of the corresponding hysteron.

3.5 Transition pathways and states

We now explore the transition pathways in a metamaterial with three defect beams under cyclic compression (Fig. 3.6). We label the defects beams as 1, 2, and 3 (left to right), their individual states as s_1, s_2 and s_3, and their collective state as $S := \{s_1, s_2, s_3\}$. In the absence of interaction, the pathways are determined by the relative ordering of the upper and lower switching strains of each hysteron [45, 50], which we denote by $\varepsilon_i^{\pm}$, where the subscript i labels the switching hysteron; if there are interactions, the situation can become more complex, and we denote the switching fields as $\varepsilon_i^{\pm}(S)$, where S is the state just before the transition [18, 44, 46, 47].

We first aim to design a metamaterial with the simplest possible pathway, such that under compression we observe a pathway $\{000\} \to \{001\} \to \{011\} \to \{111\}$, and we visit the same states in opposite order under de-

compression. Assuming that interactions can be ignored, this requires $\varepsilon_1^+ > \varepsilon_2^+ > \varepsilon_3^+$ and $\varepsilon_1^- > \varepsilon_2^- > \varepsilon_3^-$ [44, 46, 47]. We thus chose design parameters for our hysterons consistent with this ordering — the upper switching fields are mostly controlled by h and decrease for increasing h (Fig. 3.5c), and we choose dimensionless heights $\{h_1, h_2, h_3\} = \{0.23, 0.28, 0.33\}$; the lower switching fields are mostly controlled by u and increase with u, and we chose $\{u_1, u_2, u_3\} = \{0.2, 0, -0.1\}$. We refer to this as sample 'A'.
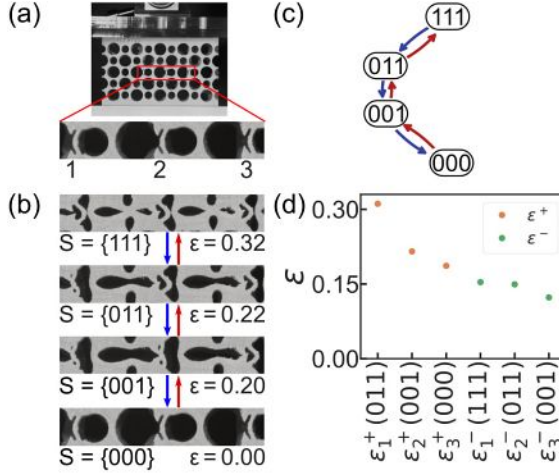

FIGURE 3.6: Robust pathways in sample A. (a) Sketch of the sample with three defects labeled 1, 2 and 3 respectively. (b) Snapshots of the defect beams during a compression/decompression cycle, showing the distinct states. (c) The transition graph of the sample A. (d) The switching fields $\varepsilon^\pm$ A ordered from large to small.

Performing cyclic compression and decompression, we observe the targeted pathway in sample A (Fig. 3.6(b)). We can collect the states and their transitions in a very simple transition graph (t-graph), where we denote the different states as nodes, and the 'up' transitions under compression, and 'down' transitions under decompression by red and blue arrows (Fig. 3.6(c)) [17, 44, 45, 48, 50]. Finally, each transition is associated with a specific value of the compression strain. We denote these as $\varepsilon_i^\pm(S)$, where the superscript $\pm$ denotes up or down transitions, the subscript i the label of the switching

hysteron, and S the initial state, just before the transition, and show these in Fig. 3.6(d). We note that although $\varepsilon_3^-(111) \approx 0.154$ and $\varepsilon_2^-(110) \approx 0.149$ are quite close, the ordering of the switching fields is consistent with our targeted ordering, and our observed pathway is robust.
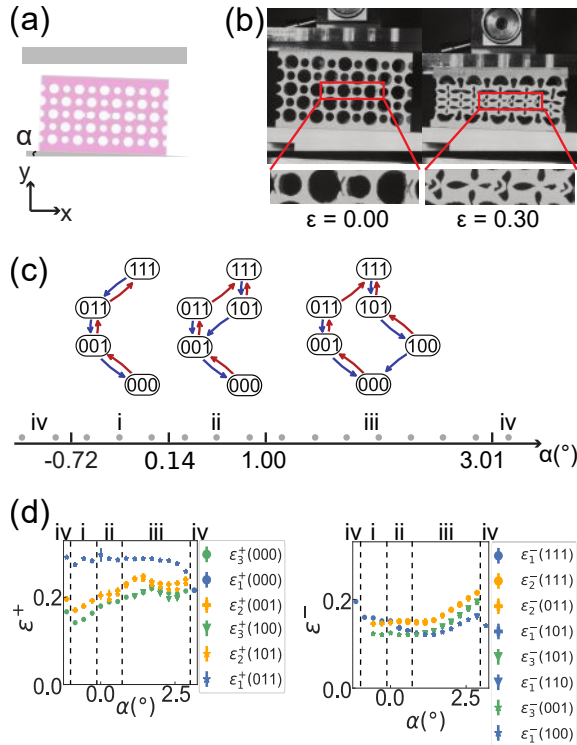
3.6 Tuning pathways by tilting

FIGURE 3.7: Tuning pathways by tilting. (a) Sketch of a sample where the bottom boundary is tilted over an angle α. (b) Snapshots of the sample A tilted by $\alpha = 1.7°$ at strains as indicated; notice the emergence of shear in the inset of the right panel. (c) As function of α, we observe three distinct pathways; gray dots indicate tilt angles where we determined the pathways, and the boundaries are estimated by bisection. (d) Corresponding critical switching fields as function of α and state S.

Spatial gradients in the driving can modify the relation between local and global driving magnitude, and allow a relative shift of the switching fields of adjacent hysterons [18]. Here we use tilting of the bottom boundary in our experiments to modify the transition pathways of a given sample (Fig. 3.7a-b). To do so, we employ a bottom plate with an adjustable tilt angle α (Fig. 3.7).

We have performed cyclic sweeps of the compression strain ε and determined the corresponding pathways and switching fields of sample A over a range of tilt angles α (Fig. 3.7c-d). We observe three distinct pathways, labeled i, ii and iii, in the range $-0.57° \leq \alpha \leq 2.86°$ (Fig. 3.7c). For tilt angle outside this range (which we label regime 'iv') one or more of the defect beams no longer exhibit sharp snapping transitions, but instead smoothly deform. Hence, they do not act as hysterons. We can detect this loss of sharp transitions and hysteresis by the absence of sharp peaks in the image differences, Δ, and attribute it to the increasing presence of shear deformations when $|\alpha|$ is large — for more discussion on shear, see below. We note that all three t-graphs are of the Preisach type, meaning that there are no avalanches, and that the sequence of hysterons switches is state independent [44, 45, 50]. In particular we note that for all pathways, the snapping sequence is the same: first hysteron 3 flips $0 \rightarrow 1$, then hysteron 2, and finally hysteron 1, yielding a sequence of states S: $\{000\} \rightarrow \{001\} \rightarrow \{011\} \rightarrow \{111\}$. However, decompressing from state $\{111\}$, we observe different unsnapping sequences in regime i, ii and iii (Fig. 3.7c). We note that while in regime i, a single sweep allows to determine all transitions, in regime ii and iii additional driving cycles are needed to establish all transitions.

In each pathway, we have determined the values of the switching fields, and plot these as function of α (Fig. 3.7d). We find that the critical switching fields of a given hysteron vary smoothly with α, and that the ordering of the upper switching fields ε_i^+ remains the same in regime i-iii, as expected. Hence, the ordering of the switching fields is consistent with the existence of the three pathways shown in Fig. 3.7c. Moreover, the lower switching fields ε_i^- cross at the boundaries between regime's i-iii. Here, two hysterons change state at the same strain, which could look like an avalanche. How-

ever, we notice that such "avalanches" are not robust to small changes in the tilt angle, and thus can be seen as degeneracies [18].

We note that the broad trends in the variation of the switching fields can be understood geometrically: in lowest order one expects an increase in α to increase the switching fields of hysteron 1, and lower those of hysteron 3. Moreover, the actual trends are more complex, due to the increasing role of shear (see right panel Fig. 3.7b) that becomes coupled to compression for $\alpha \neq 0$, and which we have observed to have a strong impact on the hysterons. Moreover, we also note that the sample is prone to global buckling, which breaks left-right symmetry, and that tilting couples to this instability and leads to shearing in the center region, which affects the behavior of the beams in each hysteron.

We measured the switching field for a given hysteron starting from two distinct states (e.g., $\varepsilon_2^+(001)$ and $\varepsilon_2^+(101)$) in regimes ii and iii, and these give insight into the presence of hysteron interactions. In the absence of hysteron interactions, the switching fields for a given hysteron should be state independent; the small but systematic deviation between $\varepsilon_2^+(001)$ and $\varepsilon_2^+(101)$ indicates the presence of hysteron interactions, which however do not lead to t-graphs that are more complex than Preisach graphs (Fig. 3.7d) [44, 45, 50].

We conclude that tilting of one of the boundaries allows to elicit multiple pathways from a single sample, and that the variation of the individual switching fields both gives an interpretation to the emergences of these pathways, as well as an experimental too to probe hysteron interactions.
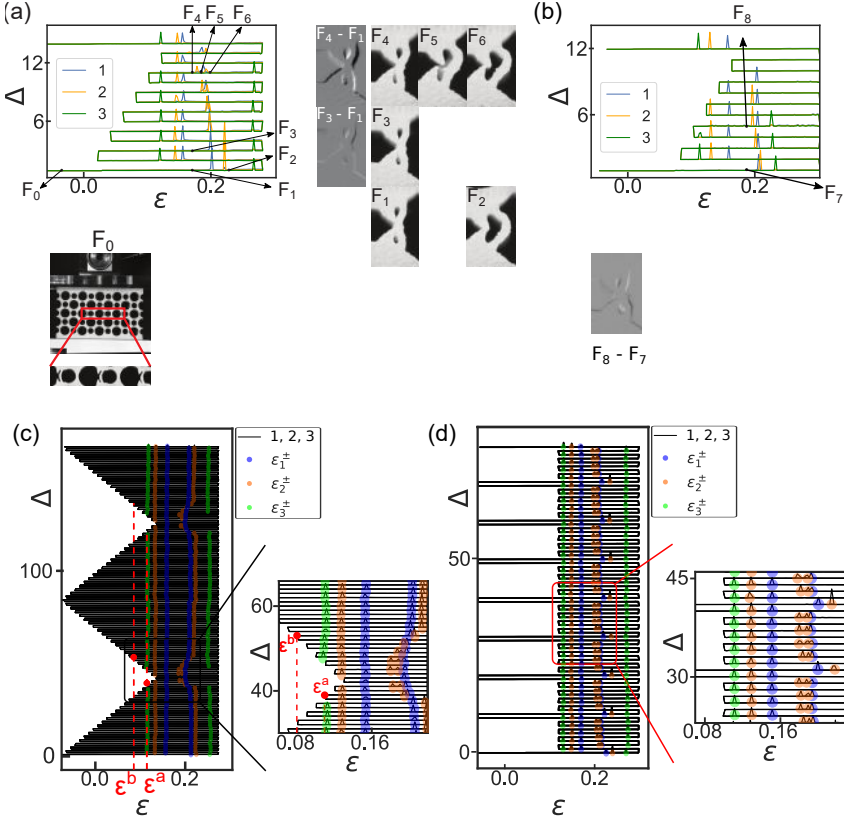
FIGURE 3.8: Snapping in sample B and additional degree of freedom. (a) The traces of the image difference Δ for multiple driving cycles where we increase the minimal compression ε^m as $0.019, 0.039, 0.059, 0.079, 0.099, 0.119$ (traces offset for clarity). Here $\alpha = 0.57°$. The location of the spikes on the upsweeps indicates the values of ε_i^+, and we observe the variation of ε_1^+ and ε_2^+ in later cycles. The labels $F1 - F6$ indicate the strains and sweeps where we took snapshots (insets). The figures $F3 - F1$ and $F4 - F1$ are difference images, which confirm that while F1 and F3 are nearly identical, F1 and F4 are distinct. (b) Image differences for $\alpha = -0.29°$ shows a weaker evolution of the switching fields ε_1^+ and ε_2^+. (c-d) Sample B, now covered in powder to reduce friction and sticking, and $\alpha = 0.57°$. Slow sweeps of ε^m evidence the presence of two critical compressions, ε_a and ε_b (c), while repeated driving at low and high values of ε^m evidences the absence of plasticity, and the presence of an additional degree of freedom with complex dynamics (d). For details, see text.

3.7 Non-hysteron degrees of freedom

For a system to be described as a collection of (interacting) hysterons, the switching fields can only depend on the current collective state, but not on other aspects of the driving history [44, 46, 47]. However, many materials when driven repeatedly can evolve in different manners, for example as they suffer from fatigue and plastic aging or exhibit visco-elastic effects [14, 21, 40, 65, 68, 69]. The presence of such additional degrees of freedom can for example be seen in the pathways of crumpled sheets that are cyclically driven [40]. As we show below, our samples also feature such additional degrees of freedom, with the relative simplicity of our system allowing us to control, reset and understand these effects.

We probe the presence of additional degrees of freedom by cyclic driving protocols, where we vary the minimum strain, ε^m over time, while probing the switching of each hysteron by monitoring the image differences. To visualize potentially slow evolution, we plot the traces of Δ as function of strain, offsetting each up and down sweep by one, as in Fig. 3.5b. We introduce a new sample B, with $\{u_1, u_2, u_3, h_1, h_2, h_3\} = \{0.2, 0, -0.1, 0.333, 0.300, 0.267\}$, i.e., with the same values of u_i as sample A, but different values of h_i. The larger values of h means pushers come into contact at lower strains than in sample A, which leads to the emergence of an additional frictional degree of freedom. Indeed, sample B is prone to deviations from purely hysteron-driven behavior, and we study it now in detail.

A first example of such a sweep is shown in Fig. 3.8a. Here we increase ε^m while keeping the maximum strain ε^M constant. We can clearly observe evolution of the upper switching fields ε_1^+ and ε_2^+, which are lowered in later cycles, and which even interchange their ordering. We stress that this happens in cycles where ε^m is low enough so that we return to state $\{000\}$; hence the evolution of ε_1^+ and ε_2^+ goes beyond simple hysteron interactions, and evidences additional degrees of freedom.

A closer inspection of the traces shows that the peak in Δ corresponding to the switching of hysteron 2 splits in two peaks — hence instead of a single snapping event, the beam undergoes two discontinuous deformations at two nearby yet distinct values of ε. To see this in more detail, we have monitored the configuration of beam 2 at given fixed $\varepsilon = 0.181$ at various sweeps (Fig. 3.8a inset). These show a clear snapping in the first sweep (frames F1, F2), and that the state of the beam in the second and first up sweep (F1, F3) are very close, as further evidenced by the absence of a clear signal in the image difference (F1-F3). However, the state of the beam on the upsweep at $\varepsilon = 0.039$ slowly evolves when the sweeps are repeated, and indeed F4 is visibly different from F1, as clearly evidenced in their image difference. In particular, we notice the emergence of shear: while the top and bottom pusher are vertically aligned in the first sweep (F1), after a few sweeps we observe misalignment and shear (F4). We find that the snapping of such a sheared beam breaks up in two events (F5 and F6), as also evidenced by the splitting of the relevant peak of Δ in two separate peaks. We believe that this shear is the main driving force between the shift of ε_1^+ and ε_2^+ that occurs long before such splitting occurs. Consistent with this, experiments performed at a lesser tilt angle show a similar but weaker evolution of the switching fields (Fig. 3.8b).

We now investigate whether shearing is slaved to the amount of compression, and potentially the hysteron state, or whether it represents (a set of) independent degrees of freedom. Moreover, we will disentangle the role of visco-plastic effects, friction and stickyness. To control the latter, we cover the samples in (baby) powder, which virtually eliminates sticking and lowers the friction, and subject the sample to a large number of sweeps with slowly varying ε^m (Fig. 3.8c). The behavior of the sample depends sensitively on the value of ε^m, and we define two critical values, $\varepsilon^a = 0.11 \pm 0.01 \approx \varepsilon_3^-$ and a smaller value $\varepsilon^b = 0.08 \pm 0.01$, where the errorbar is caused by the increment of ε^m (Fig. 3.8c). The first striking observation is that the evolution of ε_1^+ and ε_2^+ is virtually absent for sweeps where $\varepsilon^m < \varepsilon^a$. This suggests that visco-plastic effects are not the sole or main driving force, and that lowering the stickyness and friction is important. Then, when ε^m is increased beyond ε^a, we observe a rapid change in the switching fields ε_1^+ and ε_2^+, which eventually cross, after which the peak for hysteron 2 splits into two peaks, as shown before in Fig. 3.8a. One could

easily interpret the shifting of the switching fields as hysteron interactions, as when $\varepsilon^m > \varepsilon^a \approx \varepsilon_3^-$, the system does not relax to state $\{000\}$ but instead is in state $\{001\}$ when hysteron 1 and 2 flip from zero to one. However, the situation is more complex. First, the switching fields ε_1^+ and ε_2^+ evolve with the number of sweeps, without further changes in the hysteron states. Most strikingly, when we lower ε^m again, the evolution of ε_1^+ and ε_2^+ from their 'baselevel' only stops when $\varepsilon^m = \varepsilon^b < \varepsilon_3^-$, and indeed continues for a few sweeps where the system periodically returns to its $\{000\}$ state at ε^m. Hence, the evolution of the switching fields ε_1^+ and ε_2^+ evidences the presence of an additional degree of freedom, rather than direct hysteron interactions.

To clarify further that the shift of the switching fields is not visco-plastic and not a direct function of the hysteron states, we perform additional experiments where we, in succession, perform one sweep where $\varepsilon^m = 0$, so that the system can relax, and four sweeps where $\varepsilon^m = 0.099 < \varepsilon_3^-$, so that the system is driven nonlinearly but always resets to state $\{000\}$ at minimum driving. We clearly observe a different behavior of the switching fields: in the latter cycles, the peak of hysteron 2 has split and lies below that of hysteron 1, whereas in the former, the single peak of hysteron 2 lies above that of hysteron 1. Repeating these cycles evidences very little additional evolution; the behavior of the hysterons depends on ε^m, but not on the deeper history of the sample.

Based on the data in Fig. 3.8, we interpret the existence of non-hysteron degrees of freedom as follows. First, without powder, friction forces and adhesive forces introduce memory dependent contact forces between beams and pushers. For moderate ε^m these contacts, which break left-right symmetry, drive the persistent emergence of shear in the sample, as seen in the snapshots in Fig. 3.8a, which modify the switching fields and snapping behavior. When ε^m is small enough, all such contacts are broken, the shear is eliminated and the sample relaxes. For powdered samples, stickiness and friction are reduced, and the attractive and frictional forces between beam and pusher are much reduced, leading to a larger range of ε^m where the switching fields are independent of ε^m. However, for sufficiently large ε^m, opposing pushers come into contact and stay in contact over a substantial

part of the sweep, with their contacts acting as a frictional memory that directly couples to shear. Hence, in this case the switching fields ε_1^+ and ε_2^+ depend on ε^m (Fig. 3.8c-d). We note that different designs might be explored to minimize such 'memory within memory' effects. However, in many physical systems one would expect additional degrees of freedom to play a role, and so we consider our specific example of the coupling between a friction/shear degree of freedom and the hysterons to provide a testing ground for investigating such effects.

Finally, we consider how to describe this additional memory effect. We distinguish between two aspects. First, depending on the driving history, and in particular the value of ε^m with respect to ε^a and ε^b, we find that either the switching fields ε_1^+ and ε_2^+ are constant, or start to slowly evolve. Hence our data evidences the presence of a 'metabit'; when it is in state '0', ε_1^+ and ε_2^+ are constants, when it is in state '1', ε_1^+ and ε_2^+ continuously evolve with ε^m, in a manner which is beyond a hysteron description as it requires a continuous degree of freedom.

We now focus on finding a minimal model for the switching on and off of this metabit. We summarize the key features of our data in Fig. 3.9a, which summarizes our observations of the on ($M = 1$) or off ($M = 0$) state of the metabit for a sequence of five driving cycles (1)-(5). First, we note that our data can only detect a sensitivity to the value of M during upward sweeps of ε in the range of ε_1^+ and ε_2^+, which we take as $\varepsilon_1^M \leq \varepsilon \leq \varepsilon_2^M$ (indicated with a thick bar). Second, we note that a single bit-like degree of freedom is not sufficient to describe the evolution of M: both ε^a and ε^b must play a role, but we see that for ε larger than both ε^a and ε^b, M can be both zero or one. In other words, since a single sweep is not sufficient to reach $M = 1$ — rather, we need to sweep up, sweep down, and then sweep up again - capturing the evolution of the metabit requires more than a single binary degree of freedom.

We now show that our data is consistent with the scenario sketched in Fig. 3.9b, where we use four additional states $\{\tilde{S}\} = \{A, B, C, D\}$, where $M = 1$ in state C and D. We stress that these states are independent from
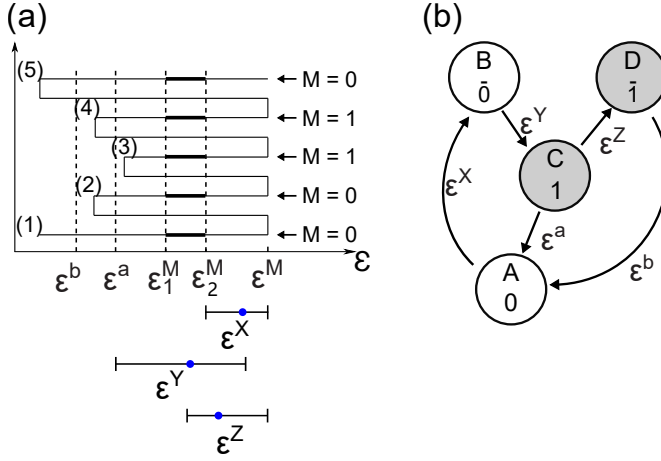
FIGURE 3.9: (a) Scenario for the switching on and off of the modifying state M. The value of M in the range $\varepsilon_1^M < \varepsilon < \varepsilon_2^M$ (bold) is indicated for upsweep (1)-(5). (b) Tentative state diagram for additional degrees of freedom beyond hysteron 1-3. The system starts out in state A, and only after a sequence of up, down and up transitions, the system can reach the modifying state D, which leads to changes in the switching fields of hysterons 1 and 2.

the state of the hysterons 1, 2 and 3. The initial state A has $M = 0$, and this is where the system returns for small ε. The transition from state A to B at ε^X needs to happen on the up-sweep. We assume that state B has $M = 0$, which requires $\varepsilon^X > \varepsilon_2^M$ (otherwise M could be one in the relevant region for all upsweeps). We then assume that there is a transition from state B to state C with $M = 1$ on the down sweep at ε^Y, which implies that $\varepsilon^a < \varepsilon^Y < \varepsilon^X$. We stress that while in this scenario $M = 1$ on (part of) the down sweeps, this does not modify ε_1^+ and ε_2^+, which only play a role on the upsweeps. Now two things can happen: if ε falls below ε^a, the system resets and returns to state A (sweep 2); but if ε remains above ε^a, state C must switch to a state D with $M = 1$, with state D only resetting back to state A for $\varepsilon < \varepsilon^b$. Hence, $\varepsilon^Z > \varepsilon^Y$. Following the transitions, we find that $M = 1$ on sweeps 3 and 4, and only resets to $M = 0$ on sweep 5, as required. Hence, the presence of two distinct state C and D which have $M = 1$ encode the observed scenario (Fig. 3.9).

To clarify the connection of states $A - D$ with the presence of the metabit M, we can also denote them as 0, $\bar{0}$, 1, and $\bar{1}$ respectively; both states 1 and $\bar{1}$ have $M = 1$, but they differ in the value of ε where they relax to state A. We then can interpret the presence of the bar as an additional binary switch, which shows that a combination of two binary degrees of freedom is sufficient to describe the evolution of the metabit M with ε. We believe that this is the simplest possible scenario consistent with our data, showing the complexity of these memory effects.

3.8   Conclusion

In this chapter we have introduced a strategy to embed mechanical hysterons into a metamaterial, and studied the ensuing pathways under cyclic compression. We showed how the hysteron properties and pathways can be tuned by the geometric design of the hysterons, and how the pathways of a given sample can be modified by tilting one of the boundaries. We investigated beyond-hysteron degrees of freedom that modify the switching fields of the hysterons. Our work is a step towards rational design of hysterons and pathways into metamaterials [4, 18, 44], and moreover highlights the importance of additional degrees of freedom [40]. Further work may extend these ideas into metamaterials where such additional degrees of freedom can be controlled, suppressed or leveraged. Moreover, we suggest that alternative designs of mechanical hysterons may allow to tune their switching fields over a wider range. Finally, we are working on methods to tune the interactions between hysterons, which can extend the range of realizable pathways dramatically [44]. We hope our work will inspire further studies on designer matter with targeted pathways.

Appendix

In Section 3.4, we have tuned $\varepsilon^\pm$ by tuning the geometry of the hysteron. Now we discuss a method to tune $\varepsilon^\pm$ without remaking the biholey meta-material: in sub-section 3.A we discuss using needles in the sample, and in sub-section 3.B we consider detachable samples that easily replace the hysterons.

3.A   Tuning $\varepsilon^\pm$ by additional pushers

In section 3.4, we showed that rubber pushers are able to modify the snapping strain. Now we consider the method of altering the pushers without re-making the sample. We notice that there is a gap between the defect beam and the original rubber pusher. By inserting a needle in the gap, the defect beam snaps earlier. In this section, we focus on additional pushers made by steel needles with a diameter of D_{add} = 1.0 mm, 1.5 mm or 2.0 mm. We first show the function of the needle, and then discuss the effect of the size of the needle.

To study how does the needle work on the defect beam, we used two samples with different original pushers, as shown in Fig. 3.10 (a) and (b) respectively. The snapshots of the samples with needles in the compression (ε = 0.00, 0.05 and 0.15) and decompression (ε = 0.07) process are shown in Fig. 3.10.

Fig. 3.10 (a) shows the role of the needles in a sample featured with a pair of small original pushers and a big gap between original pusher and the defect beam. In the compression process, the needle keeps pushing the defect beam until the defect beam snaps (ε^+ = 0.095). After snapping, the needle does not push the defect beam anymore. In the decompression process, the original pushers and needle do not push the defect beam

before unsnapping ($\varepsilon^- = 0.074$), since the gap is larger than the needle. Therefore, with the help of the original pushers, the needle only influence the snapping, and does not influence the unsnapping action. Fig. 3.10 (a) shows $\varepsilon^\pm$ as a function of D_{add}, and demonstrates that the needle greatly reduces the snapping strain.

Fig. 3.10 (b) shows the role of the needles in a sample featured with a pair of large original pushers and a small gap between original pusher and the defect beam. We see that the needle contacts the defect beam all the time in the crowded gap between the original pushers and the defect beam. Therefore, the needle influences both the snapping and unsnapping behavior of the defect beam. Sometimes, the defect beam cannot unsnap, but can only bend back slowly in the decompression process. In the experiment, whether the beam (un)snaps depend on how deep the needle is caught by the valley between the defect beam and the original pusher. In the $D_{add} - \varepsilon^\pm$ plot in Fig. 3.10 (b), we see that both the snapping strain and unsnapping strains influenced by the diameter of the needle. We observe that the defect beam does not snap but bends slowly when $D_{add} = 2$ mm. Additionally, with $D_{add} = 1.5$ mm, the bottom part of the defect beam is pushed the right slightly before the sample is compressed.

From the above information, we found that additional pushers consisting of needles mainly affect the snapping behavior and make ε^+ smaller. But in some cases, needles that are too thick prevent (un)snapping and make the defect beam bend.
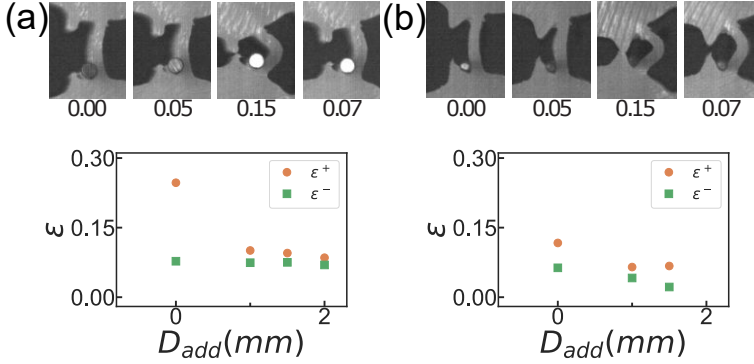
FIGURE 3.10: The role of needles for the snapping action. The samples (5×5) are characterized by $\{P, D_1, D_2, L, r, t, u\}$ = {10 mm, 10 mm, 7 mm, 6 mm, 1.2, 0.13, 0}. (a) The snapshot (D_{add} = 1.5 mm) and the $\varepsilon^{\pm}$ of the hysteron with the needle; the pusher is characterized by $\{g, A, w_t, w_b, h\}$ = {2.0 mm, 90°, 0.55 mm, 0.55 mm, 0.15}.(b) The snapshot (D_{add} = 1.0 mm) and the $\varepsilon^{\pm}$ of the hysteron with the needle; the pusher is characterized by $\{g, A, w_t, w_b, h\}$ = {0.65 mm, 60°, 0 mm, 1.9 mm, 0.26}.

3.B Detachable hysterons and composite samples

Replaceable hysterons provide an alternating method to tune the (un)snapping strain. By replacing the hysteron, we are able to tune the geometry of the sample without having to recreate the homogeneous part of the sample. So we considering the samples which consist of two parts, as shown in Fig. 3.11. The inner part we use includes the hysteron and the holes next to the hysteron, as shown in Fig. 3.11 (a). The outer part is the sample without the inner part or parts, as shown in Fig. 3.11 (b).
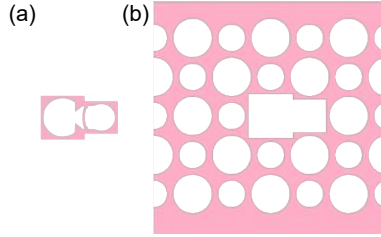
FIGURE 3.11: An example of a detachable sample. The samples (5 × 5) are characterized by $\{P, D_1, D_2, L, r, t, u, g, A, w_t, w_b, h\}$ = {10 mm, 10 mm, 7 mm, 6 mm, 1.2, 0.13, 0, 0.65 mm, 90°, 0 mm, 1.9 mm, 0.26 }. (a) Inner part. (b) Outer part.

To make the composite sample, we use one outer part and two inner parts with different original pushers, and the evolution of the inner parts under compression are shown in Fig. 3.12. As shown as the snapshots in Fig. 3.12 (a), when the sample is uncompressed (ε = 0.0), the inner part and the outer part contact each other closely. Under compression (ε = 0.1 and 0.2), the defect beam firstly creases to the left and then snaps at ε^+ = 0.127 with the help of the pushers. In the decompression process, the defect beam unsnaps at ε^+ = 0.071. We note that, between the inner part and the outer part, we see gaps near the corner of the inner part, but we do not see a gap elsewhere. The gaps near the corner of the inner part increase as ε increases. Similar to the original, simple block samples, a small pusher, $h := 1.5$, is able to help the defect beam snaps at a small strain, but ε^- is not affected by the needle, as shown in the $D_{add} - \varepsilon$ plot in Fig. 3.12 (a).

Fig. 3.12 (b) shows the behavior of the composite sample with a larger original pusher, $h := 2.6$. Similar to the simple block sample, the needle contacts the defect beam before the pusher is compressed. The thick needles, D_{add} = 1.5 mm and 2.0 mm, push the defect beam from right to left in the decompression process, as shown in the $D_{add} - \varepsilon$ plot in Fig. 3.12 (b). We note that the hysteron shown in Fig. 3.12 (b) does not snap without a needle. We observe a gap between the inner part and the outer part as the sample is compressed, so the boundaries of the hysteron in a composite sample do not rotate as much as in an simple block sample. As a result, even though the geometry of the composite sample in Fig. 3.12 (b) is the same as the

simple block sample shown in Fig. 3.10 (b), the hysteron in the composite sample does not snap without an needle.
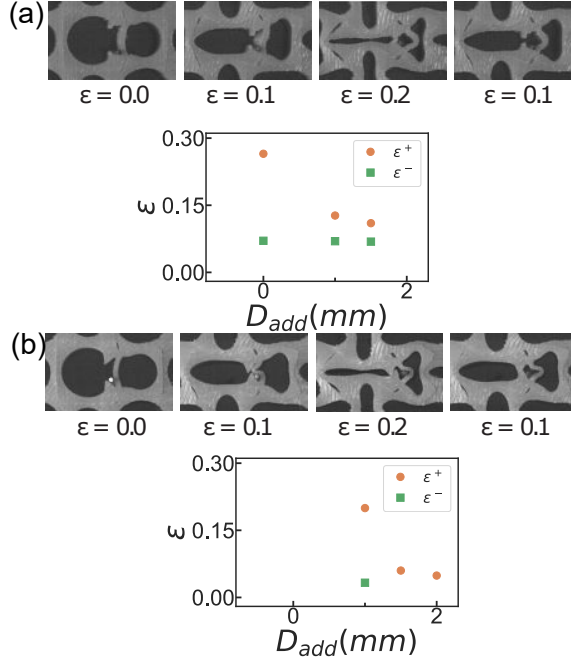

FIGURE 3.12: composite sample (5×5) with one defect beam which is characterized by $\{P, D_1, D_2, L, r, t, u\} = \{10 \text{ mm}, 10 \text{ mm}, 7 \text{ mm}, 6 \text{ mm}, 1.2, 0.13, 0 \}$. (a) The snapshot ($D_{add} = 1.0$ mm) and the $\varepsilon^{\pm}$ of the hysteron with the needle;; the pusher is charactered by $\{g, A, w_t, w_b, h\} = \{1.7 \text{ mm}, 90°, 0.5 \text{ mm}, 0.5 \text{ mm}, 0.15\}$.(b) The snapshot ($D_{add} = 1.0$ mm) and the $\varepsilon^{\pm}$ of the hysteron with the needle; the pusher is charactered by $\{g, A, w_t, w_b, h\} = \{0.65 \text{ mm}, 60°, 0 \text{ mm}, 1.9 \text{ mm}, 0.26\}$. There is no plot for ε^- at $D_{add} = 1.5$ mm and 2.0 mm due to the beam bending instead of snapping in the decompression process.